JOURNAL OF THERMOPHYSICS AND HEAT TRANSFER
Vol. 16, No. 1, January–March 2002

Capillary Limit of Evaporator Wick in Alkali Metal Thermal-to-Electric Converters

Jean-Michel Tournier* and Mohamed S. El-Genk†
University of New Mexico, Albuquerque, New Mexico 87131

Vapor anode, multitube alkali metal thermal-to-electric converters are being developed for potential use in space and terrestrial electric power generation. In these converters, the capillary pressure head produced in the evaporator wick circulates the sodium working fluid. A two-dimensional, thermal–hydraulic model of the porous evaporator wick and of the liquid sodium return artery is developed and thermally coupled to an integrated model of a five-beta″-alumina solid electrolyte (BASE) tube, stainless-steel sodium converter (PX-3A), and an eight-tube, Mo–41% Re sodium converter. Results showed that the capillary limit in the evaporator wick of the PX-3A converter is reached at zero electrical current, when the thermal input power to the converter exceeds 16 W, or the hot-side temperature exceeds 1136 K. For the Mo–41% Re converter, these values are 22 W and 1150 K, respectively. Before reaching the capillary limit, however, two or more of the following temperature limits occurred in both converters: 1) the TiNi metal–ceramic braze joints' temperature exceeded 1123 K, 2) the evaporator wick surface temperature exceeded 1023 K, or 3) the temperature difference between the cold end of the BASE tubes and the evaporator wick surface was less than +20 K.

Nomenclature

A	=	surface area, m^2
a_{cc}	=	accommodation coefficient for evaporation/condensation
B	=	charge-exchange coefficient, $A \cdot K^{1/2}/Pa \cdot m^2$
C	=	inertia coefficient, Eqs. (16b) and (17)
C_p	=	specific heat, $J/kg \cdot K$
D	=	thermal conductance, $W/m^2 \cdot K$
F	=	Faraday's constant, 96,485 C/mol
G_E	=	geometric factor for pressure losses in electrode
g	=	gravity acceleration, 9.81 m/s^2
h	=	enthalpy, J/kg
I	=	electrical current, A
K	=	permeability, Eqs. (16b) and (17), m^2
k	=	thermal conductivity, $W/m \cdot K$
M	=	molecular weight of sodium, 23 g/mole
$\dot{m}''_{ev}$	=	vaporization mass flux, $kg/m^2 \cdot s$
$\dot{m}_I$	=	sodium flow rate in the converter, kg/s
N_B	=	number of beta″-alumina solid electrolyte (BASE) tubes
P	=	pressure, Pa
P_e	=	electrical power output, W_e
P_{sat}	=	sodium saturation pressure, Pa
q	=	area-averaged velocity in wick, m/s
Q	=	conduction heat flow rate, W
Q_{in}	=	input thermal power, W
Q^{rad}	=	net rate of radiant heat loss, Eq. (2), W
R_c	=	radius of curvature, m
R_g	=	perfect gas constant, 8.314 $J/mol \cdot K$
R_L	=	external load resistance, Ω
R_p	=	effective pore radius of evaporator wick, m
r	=	radial coordinate, m
T	=	temperature, K
t	=	time, s
V_L	=	external load voltage, V
Vol	=	volume, m^3
z	=	axial coordinate, m
α_p	=	vapor volume fraction in porous wick
Γ	=	conduction/advection heat flux, W/m^2
ΔP	=	pressure head/drop, Pa
ΔR_i	=	radial width of numerical mesh, m
ΔT	=	temperature margin $(T_B - T_{ev})$, K
Δt	=	discretization time step, s
ΔZ_j	=	axial width of numerical mesh, m
ε	=	wick volume porosity
θ	=	apex half angle of cone
μ	=	dynamic viscosity, $kg/m \cdot s$
μ_c	=	cosine of contact angle, R_p/R_c
ρ	=	density, kg/m^3
σ_L	=	liquid surface tension, N/m
$\chi_{i,j}$	=	evaporation coefficient, Eq. (6), $a_{cc}(M/2\pi R_g T_{i,j})^{1/2}$

Subscripts/Superscripts

a	=	anode side of BASE
B	=	cold end of BASE tubes
c	=	cathode side of BASE
cap	=	capillary pressure
cd	=	condenser
eff	=	effective
ev	=	evaporator wick surface
hot	=	hot side of converter
i	=	radial discretization number
j	=	axial discretization number
L	=	liquid phase
m	=	solid matrix of wick
n	=	temporal discretization number
V	=	vapor phase
$*$	=	best estimate of new-time variable
$'$	=	correction

Received 26 December 2000; revision received 9 August 2001; accepted for publication 30 August 2001.

*Research Assistant Professor, Institute for Space and Nuclear Power Studies. Member AIAA.

†Regents' Professor of Chemical and Nuclear Engineering and Director, Institute for Space and Nuclear Power Studies; mgenk@unm.edu. Associate Fellow AIAA.

Introduction

SEVERAL stainless-steel vapor anode, multitube alkali metal thermal-to-electric converters (AMTECs), designed and assembled by Advanced Modular Power Systems, Inc., have been tested

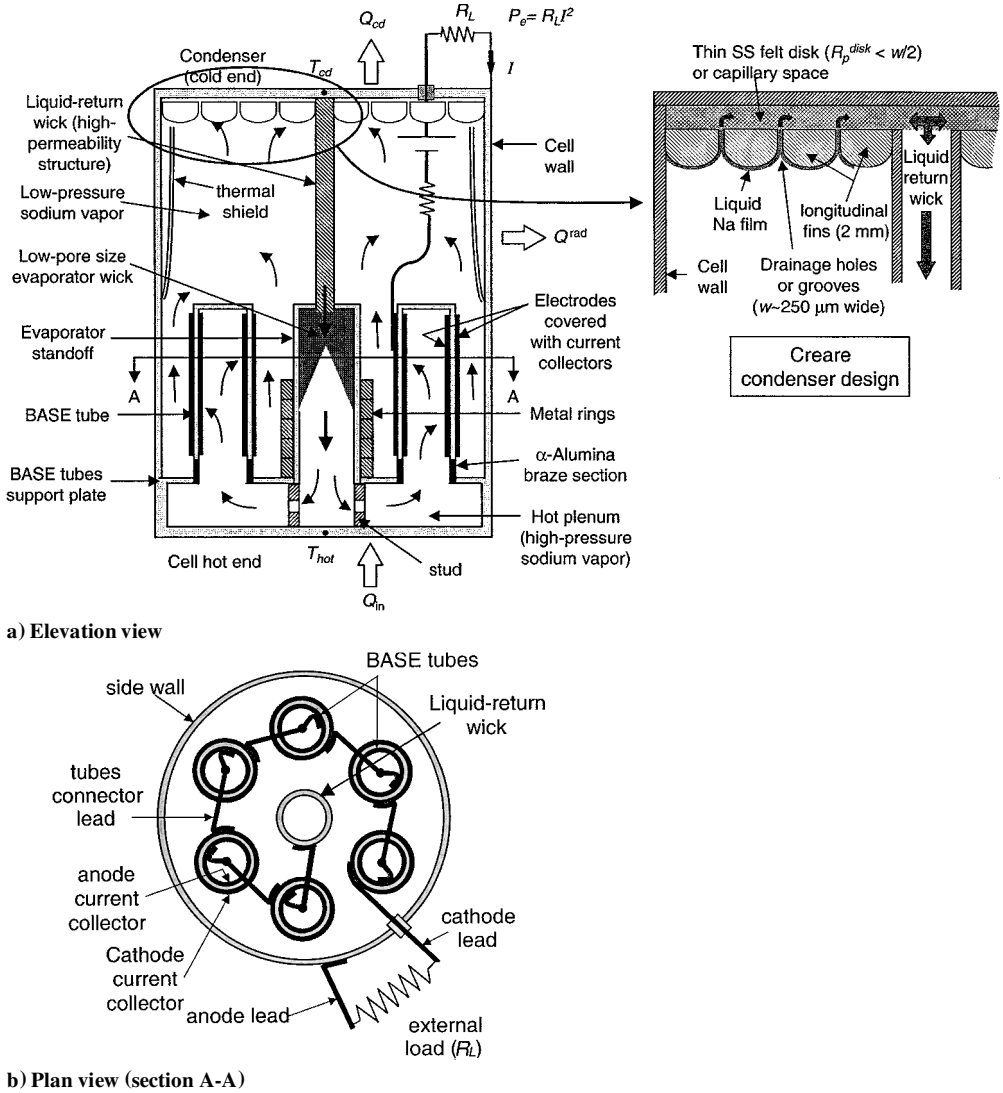

Fig. 1 Cross-sectional views of a typical vapor anode AMTEC converter with six BASE tubes connected in series (not to scale).

in vacuum at the U.S. Air Force Research Laboratory (AFRL).[1] A typical converter measures ~4 cm in diameter and ~10 cm in height; it weighs ~160 g and contains from five to eight beta″-alumina solid electrolyte (BASE) tubes of nominal composition $Na_{5/3}Li_{1/3}Al_{32/3}O_{17}$ (Ref. 2). The BASE material is a dense, microcrystalline, sintered ceramic, which has very high ionic conductivity and very low electronic conductivity.[2] The BASE tubes are arranged in a circle inside the cylindrical enclosure of the converter (Fig. 1) to minimize parasitic thermal losses by radiation to the wall. In addition, the BASE tubes are connected electrically in series to produce an output voltage above 2.5 V. When operated at a hot-side temperature of 1173 K and a condenser temperature of 623 K, the stainless-steel converters tested at AFRL delivered 3–5 We at 2.0–3.5 V dc (Ref. 1). The estimated efficiency of these converters ranged from 11 to 14%.

A vapor anode AMTEC converts heat to electricity by using the unique characteristics of the BASE Na^+ conducting ceramic. This ceramic membrane conducts sodium ions, but is an electrons insulator. An electrochemical potential is developed when sodium vapor is present on both sides of the BASE, but at different pressures. The liquid sodium in the high-pressure region (20–90 kPa) evaporates from a porous wick, and the vapor flows to the surface of the BASE (anode) where it ionizes, and the ions diffuse through the BASE to the low-pressure (<100 Pa) side (cathode). The freed electrons in the anode porous electrode are captured by the current collector, to flow through an external load under the potential differential developed to balance the pressure difference across the BASE. The electrons returning from the external load recombine with the sodium ions emerging on the cathode side of the BASE, to form neutral sodium atoms. These atoms evaporate from the cathode side of the BASE, diffuse through the porous electrode and metallic current collector, and flow as low-pressure vapor to the remote condenser of the converter, where they condense in its porous structure. The sodium liquid then flows from the condenser through a porous, liquid sodium return artery (LSRA) to the evaporator wick, and the process is repeated.

In this paper, a two-dimensional thermal–hydraulic model of the evaporator wick and the LSRA of the AMTEC converter (Fig. 1) is developed and thermally coupled to an integrated converter computer code APEAM[3–5] to investigate the effect of the cone angle of the evaporator wick, the converter's hot-side temperature, and electric current on the capillary limit in the wick. In addition, the question of whether the capillary limit is reached at a higher heat input (or hot-side temperature) than other operational temperature limits is investigated. Calculations are performed for a five-BASE-tube, stainless-steel converter, known as PX-3A (Ref. 1) and a refractory Mo–41%Re converter having eight BASE tubes.[6,7] The latter uses $W/Rh_{1.5}$ electrodes, weighs 209 g, and delivers 7.4 W_e at an estimated efficiency of ~16% and a load voltage of 3.0 V, without exceeding any of the operation temperature limits. The Mo–41%Re converter alleviates concerns of incompatibility of the stainless-steel structure in multitube converters with the sodium working fluid

Table 1 Design and performance parameters of the PX-3A stainless-steel converter and Mo–41%Re converter

Design and performance parameters	PX-3A type, SS converter	Mo–41%Re converter
Design parameters		
Overall converter mass, g	~140	209
Converter diameter, mm	31.75	41.27
Converter height, mm	101.6	125.3
Condenser type/material	Creare/SS	Creare/Mo–41Re
LSRA material/diameter, mm	SS/3.2	Mo/3.2
LSRA length, mm	~60	~68
Evaporator material/elevation, mm	SS/5.2	Mo/12.5
Standoff material/thickness, mm	SS/0.71	Mo–41Re/0.71
Standoff inner diameter, mm	4.9	11.9
Rings material/thickness, mm	Ni/1.1	None
Conduction stud material/area, mm^2	SS/38	Mo–41Re/10
Hot-wall material/thickness, mm	SS/0.71	Mo-41Re/0.2
Cold-wall material/thickness, mm	SS/0.101	Mo–41Re/0.101
Thermal radiation shield/material	Cylindrical/SS	Cylindrical/Mo
Number of BASE tubes	5	8
BASE tube o.d./thickness, mm	7.62/0.508	7.62/0.508
Length of BASE tube assembly, mm	32	50
Electrodes material/length, mm	TiN/25.4	$WRh_{1.5}$/38.1
Electrode area per tube, mm^2	608	912
Charge-exchange current coefficient B, $A \cdot K^{1/2}/m^2 \cdot Pa$	80	90
Electrode pressure loss coefficient G_E	50	10
Collector/BASE contact resistance, $\Omega \cdot cm^2$	0.09	0.06
Performance at peak electric power output		
Hot-side temperature, K	1173	1173
Condenser temperature, K	623	640
BASE tubes braze temperature, K	1150	1123
Evaporator surface temperature, K	1070	987
Temperature margin ΔT, K	~0	+41
Electrodes current density, A/cm^2	0.42	0.29
External load voltage, V	1.83	2.88
Electrical power output, W_e	4.7	7.5
Converter conversion efficiency, %	14.0	16.1
Converter specific mass, g/W_e	29.8	27.9

and with the TiN electrodes and concerns of oxygen pickup and embrittlement of Nb–1%Zr during prelaunch assembly and high-temperature testing.[6,7] A comparison of the design characteristics and the performance parameters of the PX-3A and Mo–41%Re converters are given in Table 1.

Design and Operation of Vapor Anode AMTEC

In the stainless-steel (SS) converters, the BASE tubes and the housing of the evaporator assembly (or standoff) are brazed to a SS support plate using TiNi brazes (Fig. 1). The BASE tubes and the evaporator wick housing divide the enclosure of the converter into the high sodium vapor pressure (20–90 kPa) cavity and the low sodium vapor pressure (<100 Pa) cavity. The high-pressure (or anode) and the low-pressure (or cathode) sides of the BASE are covered with thin porous titanium nitride (TiN) electrodes (2–25 μm thick on the anode side and 0.5–2 μm thick on the cathode side) and molybdenum current collectors. The anode electrode allows sodium atoms to diffuse to the surface of the BASE, where they are ionized. The anode electrode also provides a conduction path for the freed electrons to diffuse to the metal current collector. The pressure differential across the BASE membrane is balanced by the electrical potential developed by the diffusing sodium ions (Na^+) through the isothermal, thin BASE solid electrolyte (~0.5 mm thick). The developed electric potential is proportional to the logarithm of the ratio of the sodium vapor pressures at the anode and cathode sides. The terminal voltage of the converter equals the sum of the electric potentials developed across the BASE tubes minus the internal electrical losses in the BASE, electrodes, current collectors, and electric leads (Fig. 1).

The emerging sodium ions at the cathode recombine with the electrons circulating from the external load. The resulting low-pressure vapor (~20–100 Pa) diffuses through the cathode electrode and flows to the remote condenser (~600 K), where it condenses into liquid, giving up the latent heat of condensation. The latter is rejected through the outer surface of the condenser. Liquid sodium is circulated from the porous condenser wick through the LSRA to the evaporator wick, by the capillary pressure head developed at the surface of the wick. At the evaporator wick surface, liquid sodium absorbs the latent heat of vaporization, converting into high-pressure vapor (20–90 kPa). The heat of evaporation is provided by heat conduction from the support plate through the evaporator standoff wall and the surrounding metal rings (Fig. 1).

Heat also flows to the BASE tubes mostly by conduction from the hot plate (Fig. 1). The metal stud enhances heat conduction to the support plate (Fig. 1). A porous Creare-type condenser wick is used to maintain a continuous thin film of liquid sodium on its surface, effectively reflecting ~95% of escaping thermal radiation toward the interior of the converter.[8] The specially shaped longitudinal fins (~2 mm wide) of the Creare-type condenser provide a capillary force an order of magnitude larger than the hydrostatic force at Earth gravity, forcing liquid sodium to spread uniformly on the surface. The small grooves between fins (~250 μm wide) facilitate the condensate flow to an underlying felt wick or small capillary space (see insert in Fig. 1a). To reduce parasitic heat losses by thermal radiation from the BASE tubes and by reflection from the condenser surface, a circumferential, SS, thermal radiation shield is placed on the inside of the wall above the BASE tubes (Fig. 1). The inner surface of the shield may be covered by a highly reflective coating, such as rhodium. Because the shield temperature is typically much higher than that of the condenser, condensation of sodium vapor on its surface is nil.

The porous structure of the condenser is thermal hydraulically coupled to the LSRA, a porous metal wick structure that extends to the evaporator wick (Fig. 1). The LSRA is made of SS felt that is sintered at 1173 K or above. To minimize pressure losses, the LSRA has a relatively large pore size (10–25 μm) and a permeability $> 10^{-12}$ m^2. Early SS converters had a flat evaporator wick, $\theta = 90$ deg (Ref. 1). Later converters had conical evaporators ($\theta < 90$ deg) to increase the surface area for evaporation and avoid incipient dryout. However, to the best of the authors' knowledge, neither modeling nor calculations have been reported in the literature that assess the effect of the cone angle of the evaporator wick on the operation and the capillary limit of PX-type converters.

The evaporator wick of the PX-3A converter, made of SS felt that is sintered at 1173 K or above, has a very small pore size (≤ 5 μm) to provide sufficient capillary pressure head to circulate the sodium working fluid and to balance the hydraulic pressure losses in the converter. These losses include those in the LSRA and condenser, the high- and low-pressure cavities, the BASE, and the anode and cathode electrodes. At steady state, the sum of the pressure losses equals the capillary pressure head developed at the evaporator wick surface. The pressure losses in the converter are functions of the sodium flow rate (or electric current), which depends on the external load resistance.

The capillary pressure head generated at the surface of the evaporator wick is directly proportional to the surface tension of liquid sodium at the local surface temperature, divided by the radius of curvature of the liquid meniscus in the surface pores. Increasing the hot-plate temperature (or the heat input) increases the temperature of the evaporator surface and, hence, the sodium vapor pressure, but decreases the surface tension. On the other hand, decreasing the external load resistance increases the electrical current and, consequently, the sodium mass flow rate. The increase in the sodium flow (or evaporation) rate reduces the surface temperature of the evaporator wick and increases the surface tension. Conversely, the increase in the evaporation rate of sodium decreases the radius of curvature of the liquid meniscus in the surface pores of the evaporator wick. The net effect of decreasing surface tension and radius of curvature would be an increase in the capillary pressure head. When the radius of curvature equals the effective pore radius of the evaporator wick (~4 μm), the capillary limit or incipient dryout is reached.

In addition to the capillary limit, there are three operational temperature limits that apply to the operation of the vapor anode AMTEC converters. These limits should not be exceeded to ensure long operation lifetime of the converter, up to 10 or even 15 years. First, to avoid sodium condensation inside the BASE tubes, which could eventually short the BASE electrodes, the temperature at the cold end of the BASE should be more than 20 K higher than the evaporator wick surface temperature, $\Delta T > 20$ K (Ref. 9). This can be achieved by the proper selection of the dimensions of the evaporator standoff wall and conduction rings (length and thickness, see Fig. 1a). Second, to avoid volatilization of the metallic elements in the TiNi brazes, hence, cracking or degradation of the electrical and thermal properties of the brazes,[9] the temperature of the braze of the BASE to the metal support plate should be kept below 1123 K. This pressure-tight braze structure electrically insulates the BASE tubes from the support plate, while readily conducting heat from the latter to the former. Third, to avoid an increase in the pore size in the evaporator wick due to grain growth, it is desirable to maintain the molybdenum wick surface temperature at or below 1023 K (750°C).

In this paper, the conditions for reaching these limits, as well as the capillary limit in the evaporator wick of the converter, are investigated and compared. The next section describes the LSRA and the evaporator wick model developed in this work.

Model Description

The developed two-dimensional, thermal–hydraulic model of the LSRA and of the evaporator wick solves the enthalpy balance equation after accounting for thermal radiation exchange with the surrounding structure in the converter, heat conduction through the evaporator standoff wall and the surrounding metal rings, and heat losses by conduction in the LSRA to the condenser. The thermal model in the AMTEC APEAM code[4] is used to evaluate the thermal radiation exchange between both the LSRA and the evaporator wick and the surrounding structure of the converter. The calculated temperatures are functions of the converter design, the hot-side and condenser temperatures, and the external load resistance, which determines the flow rate of the sodium working fluid. Whereas the latter is calculated, the former parameters are input to the APEAM/evaporator wick model.

In addition to the sodium flow rate, the capillary pressure head and the radius of curvature of the liquid meniscus in the surface pores of the evaporator wick need to be calculated. Three equations are solved for these quantities. The first equation is the overall momentum balance, which equates the sum of pressure losses in the converter to the capillary pressure head developed at the surface of the evaporator. The pressure losses in the converter are determined by the present APEAM/wick model. The second equation is the Young–Laplace relation at the liquid–vapor interface in the pores at the surface of the evaporator wick. This equation expresses the capillary pressure head in terms of the surface tension and the curvature of the liquid meniscus in the surface pores of the evaporator wick. The third equation expresses the mass flow rate of sodium in terms of the terminal voltage of the converter. This voltage equals the sum of the potentials developed in the BASE tubes minus electrical losses. APEAM calculates all of the electrical losses in the converter in terms of the electric current and sodium vapor pressures at the BASE/electrode interfaces.[5] Because of the dependence of the thermophysical and electrical properties of the structure materials and of the sodium working fluid on temperature, as well as the complexity of the thermal radiation exchange between the LSRA and evaporator wick with the surrounding BASE tubes and converter wall, the current problem is highly nonlinear. The efficient iterative solution procedure, developed to solve the governing and constituent equations of the problem, is described later.

Governing Equations

The present transient, two-dimensional thermal–hydraulic model calculates the local sodium vaporization/condensation rates and the local curvature of the liquid meniscii in the surface pores of the evaporator wick. The heat transfer by radiation between the hot plate and the interior of the evaporator cavity is neglected in this analysis (Fig. 1). Previous results have shown that this quantity is small compared to that by conduction in the evaporator standoff wall and to the heat removed by the sodium evaporation at the evaporator wick surface.[4]

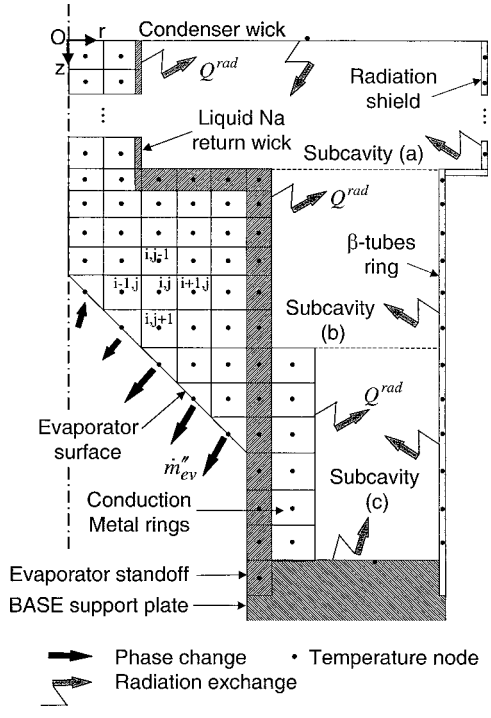

Fig. 2 Computation grid in a conical evaporator and liquid sodium return artery.

The momentum and energy balance equations for the evaporator wick and LSRA are very complex and highly nonlinear. These equations and the associated boundary conditions are discretized on a two-dimensional (staggered) cylindrical grid (Fig. 2) using the control-volume approach.[10] The local density, pressure, temperature, and enthalpy of the liquid-saturated porous structures of the evaporator and LSRA are calculated at the centers of the control volumes, whereas the mass fluxes of the sodium working fluid are calculated at the surfaces of the control volumes. In all subsequent equations, the superscripts (n) and $(n+1)$ refer to the old and new time steps, respectively. Given a variable best estimate, for example, temperature T^*, the numerical solution seeks a primed correction field T' such that $T^{n+1} = T^* + T'$.

The homogeneous, volume-averaged enthalpy conservation equation in the liquid-saturated porous structures of the evaporator and LSRA can be written as[11]

$$\frac{\partial}{\partial t}[\varepsilon(\rho h)_L + (1-\varepsilon)(\rho h)_m] + \mathrm{div}[(\rho h)_L \boldsymbol{q}] = \mathrm{div}[\bar{\bar{k}}_{\mathrm{eff}} \nabla T] \quad (1)$$

This equation also applies to the nonporous standoff wall and the metal rings by substituting $\varepsilon = 0$ and $\boldsymbol{q} = 0$. The enthalpies of the liquid and solid matrix are linearized in terms of temperature using the specific heat of the respective phases. Integrating Eq. (1) over a control volume (i, j) gives[10]

$$\frac{\varepsilon \mathrm{Vol}}{\Delta t}\left\{(\rho h)^*_L - (\rho h)^n_L + \left[(\rho C_p)^*_L + h^*_L\left(\frac{\partial \rho_L}{\partial T}\right)^*_p\right]T'\right\}$$

$$+ \frac{(1-\varepsilon)}{\Delta t}\mathrm{Vol}\,\rho_m\left[(h)^*_m - (h)^n_m + (C_p)^*_m T'\right]$$

$$+ Q^{\mathrm{rad}}_{i,j} + (A_r\Gamma_r)^{n+1}_{i,j} - (A_r\Gamma_r)^{n+1}_{i-1,j}$$

$$+ (A_z\Gamma_z)^{n+1}_{i,j} - (A_z\Gamma_z)^{n+1}_{i,j-1} = 0 \quad (2)$$

The radial conduction/advection heat flux $\Gamma_r^{i,j}$ at the interface (i, j) between the control volumes (i, j) and $(i+1, j)$, can be expressed as

$$(\Gamma_r)_{i,j}^{n+1} = (D_r)_{i,j}^* \left(T_{i,j}^{n+1} - T_{i+1,j}^{n+1}\right) + (\rho_L q_r)_{i,j}^* \times \left\lfloor (\varphi_r)_i \left(h_L^{n+1}\right)_{i,j} + (1-\varphi_r)_i \left(h_L^{n+1}\right)_{i+1,j} \right\rfloor \quad (3a)$$

where

$$(D_r)_{i,j}^* = 2\left[\frac{\Delta R_i}{(k_{\text{eff}})_{i,j}^*} + \frac{\Delta R_{i+1}}{(k_{\text{eff}})_{i+1,j}^*}\right]^{-1}$$

$$(\varphi_r)_i = 1 - \frac{\pi\left[r_i^2 - (r_i - \Delta R_i/2)^2\right]}{\pi\left(r_{i+1}^2 - r_i^2\right)} \quad (3b)$$

Similarly, the axial heat flux $\Gamma_z^{i,j}$ at the interface (i, j) between control volumes (i, j) and $(i, j+1)$ is

$$(\Gamma_z)_{i,j}^{n+1} = (D_z)_{i,j}^* \left(T_{i,j}^{n+1} - T_{i,j+1}^{n+1}\right) + (\rho_L q_z)_{i,j}^* \times \left\lfloor (\varphi_z)_j \left(h_L^{n+1}\right)_{i,j} + (1-\varphi_z)_j \left(h_L^{n+1}\right)_{i,j+1} \right\rfloor \quad (4a)$$

where

$$(D_z)_{i,j}^* = 2\left[\frac{\Delta Z_j}{(k_{\text{eff}})_{i,j}^*} + \frac{\Delta Z_{j+1}}{(k_{\text{eff}})_{i,j+1}^*}\right]^{-1}, \qquad (\varphi_z)_j = \frac{\Delta Z_j}{\Delta Z_j + \Delta Z_{j+1}} \quad (4b)$$

Because of the high thermal conductivity and low mass flow rate of liquid sodium (typically $\dot{m}_I < 20$ g/h), the heat transfer in the evaporator wick and LSRA is dominated by axial conduction (sodium Peclet number < 0.08). For a control volume (i, j) that does not have a $(i+1, j)$ neighboring control volume, $(\Gamma_r)_{i,j} = 0$, and along the symmetry axis of the evaporator wick, $(\Gamma_r)_{0,j} = 0$. For the surface elements of the evaporator wick (see Fig. 2)

$$(\Gamma_r)_{i-1,j} = 0, \qquad (\Gamma_z)_{i,j} = (A_{\text{ev}} \dot{m}''_{\text{ev}} h_V)_{i,j} \quad (5)$$

Local Evaporation/Condensation Rates

The local evaporation/condensation rate at the surface of the evaporator wick is expressed as

$$(\dot{m}''_{\text{ev}})_{i,j} = a_{cc}(M/2\pi R_g T_{i,j})^{\frac{1}{2}} [P_{\text{sat}}(T_{i,j}) - P_a] = \chi_{i,j}[P_{\text{sat}}(T_{i,j}) - P_a] \quad (6)$$

where $T_{i,j}$ is the wick surface node temperature. In an evacuated, clean system, which is assumed to be the case in AMTEC, the accommodation coefficient, a_{cc} for liquid metals is taken as unity.

Vapor Pressure in Evaporator Cavity

The vapor pressure in the evaporator cavity, P_a, in Eq. (6) is a function of the sodium vapor flow rate through the BASE tubes, $\dot{m}_I$. Thus, the mass balance in the evaporator cavity gives

$$\text{Vol}_a \frac{\partial \rho_V}{\partial t} + \dot{m}_I = \int_{\substack{\text{cone}\\ \text{surface}}} \dot{m}''_{\text{ev}} \, \text{d}A_{\text{ev}} \quad (7)$$

When it is assumed that sodium vapor is a perfect gas, Eq. (7) is discretized as

$$\frac{\text{Vol}_a M}{R_g T_V} \times \frac{P_a^{n+1} - P_a^n}{\Delta t} - \sum_{\substack{\text{cone}\\ \text{surface}}} A_{\text{ev}}^{i,j} \chi_{i,j} \left[P_{\text{sat}}(T_{i,j}) - P_a^{n+1}\right] = -\dot{m}_I \quad (8)$$

Rearranging Eq. (8) gives the new-time, sodium vapor pressure in the evaporator cavity as

$$P_a^{n+1} = \frac{\sum_{\substack{\text{cone}\\ \text{surface}}} A_{\text{ev}}^{i,j} \chi_{i,j} P_{\text{sat}}(T_{i,j}) + \Lambda P_a^n - \dot{m}_I}{\sum_{\substack{\text{cone}\\ \text{surface}}} A_{\text{ev}}^{i,j} \chi_{i,j} + \Lambda} \quad (9)$$

where $\Lambda = \text{Vol}_a M/(R_g T_V \Delta t)$. The vapor temperature T_V is taken equal to that of the BASE support plate, minimally affecting P_a. At steady state, $P_a^{n+1} = P_a^n$ and is given by Eq. (9) when $\Lambda = 0$. To enhance the computational efficiency of the numerical scheme, the vapor enthalpy in Eq. (5) is linearized as

$$(\dot{m}''_{\text{ev}} h_V)_{i,j}^{n+1} = (\dot{m}''_{\text{ev}} h_V)_{i,j}^* + (\dot{m}''_{\text{ev}})_{i,j}^* \left(C_p^L + \frac{\partial h_{LV}}{\partial T}\right)^*_{i,j} T'_{i,j} + (h_V)_{i,j}^* \times \sum_{\substack{\text{cone}\\ \text{surface}}} \frac{\partial (\dot{m}''_{\text{ev}})_{i,j}^*}{\partial T_{k,l}} \times T'_{k,l} \quad (10)$$

The partial derivatives of Eqs. (6) and (9) with respect to temperatures give

$$\frac{\partial (\dot{m}''_{\text{ev}})_{i,j}^*}{\partial T_{k,l}} = \left(\frac{\partial \chi_{i,j}}{\partial T_{k,l}}\right)^* \left[P_{\text{sat}}(T_{i,j}^*) - P_a^*\right] + \chi_{i,j}^* \left[\left(\frac{\partial P_{\text{sat}}(T_{i,j})}{\partial T_{k,l}}\right)^* - \left(\frac{\partial P_a^{n+1}}{\partial T_{k,l}}\right)^*\right] \quad (11)$$

These derivatives are used in the third term on the right-hand side of Eq. (10). This linearization of Eq. (6) is a key to obtaining a fast-converging solution.

Thermal Radiation Losses

The term $Q_{i,j}^{\text{rad}}$ in Eq. (2), at the surface of the control volumes in the metal rings and in the evaporator standoff and LSRA wall (Fig. 2), accounts for the net heat exchange by radiation within the low-pressure cavity of the converter. This cavity is divided into three radiatively coupled, elementary regions (Fig. 2). The surface of each control volume facing the low-pressure cavity is given an absolute number k, and all radiation view factors are calculated using closed-form solutions.[4] Equation (2) is solved numerically for given temperatures of the BASE support plate and of the condenser. The temperatures of the nodes in the BASE tubes, converter wall, and heat shield are calculated by APEAM and used as input boundary conditions to the present thermal radiation losses model. In this model, all surfaces are assumed gray and diffuse. To solve Eq. (2) for the temperatures of the nodes in the evaporator and LSRA, the net radiant energy loss $Q_{i,j}^{\text{rad}}$ is expressed as a function of temperatures and is linearized using the procedure detailed in Ref. 4.

Effective Thermal Conductivity

The effective thermal conductivities of the evaporator wick and the LSRA in Eqs. (3b) and (4b) are calculated as functions of the local volume porosity and the conductivities of the liquid sodium and solid matrix. The sintered metal wicks of the evaporator and the LSRA are made of packed metal spheres having a radius R_s. For a sintered metal wick with a large contact area R_c, the effective conductivity is calculated as[12]

$$\frac{k_{\text{eff}}}{k_m} = \frac{\pi}{8}\left(\frac{R_c}{R_s}\right)^2 + \left[1 - \frac{\pi}{8}\left(\frac{R_c}{R_s}\right)^2\right] \times \left[\frac{k_L}{\varepsilon' k_m + (1-\varepsilon') k_L}\right] \quad (12a)$$

where

$$\varepsilon' = \varepsilon\left[1 - \frac{\pi}{8}\left(\frac{R_c}{R_s}\right)^2\right]^{-1} \quad (12b)$$

$$\varepsilon = \frac{\pi}{6}\left\{1 - \left(\frac{R_c}{R_s}\right)^2\left[2 - \sqrt{1 - \left(\frac{R_c}{R_s}\right)^2}\right]\right\} \times \left[1 - \left(\frac{R_c}{R_s}\right)^2\right]^{-\frac{2}{3}} \quad (12c)$$

In Eq. (12a), ε' can be represented within $\pm 1\%$ using the following empirical relationship:

$$\varepsilon' = 1.19 \times \varepsilon^{0.946} - 2.65 \times \varepsilon^{4.81} \tag{13}$$

In this work, the volume porosity of the LSRA is taken as 0.64 and that of the evaporator wick as 0.42, for both the SS and the refractory converters.

Circulation of Sodium Working Fluid and the Capillary Limit

At steady state, the developed capillary pressure head at the surface of the evaporator wick equals the sum of pressure losses in the converter

$$\Delta P_{\text{cap}} = 2\sigma_L / R_c = \Delta P_{\text{cell}} + \Delta P_{\text{wick}} \tag{14}$$

The pressure losses include those in the LSRA and the evaporator wick, ΔP_{wick}, and in the anode and cathode cavities of the converter, ΔP_{cell}. The latter is due to sodium evaporation at the wick surface and condensation at the condenser, sodium vapor flow to the BASE anode, isothermal expansion of sodium ions through the BASE, and the sodium vapor flow from the BASE cathode to the condenser (Figs. 1 and 3). At the relatively low mass flow rates (<25 g/h) typically encountered in AMTECs, the pressure losses due to the sodium flow in the condenser wick and the evaporation and condensation at the evaporator wick and condenser surfaces are negligible. The evaporator wick and LSRA model calculates ΔP_{wick}, whereas ΔP_{cell} is calculated by APEAM.[3]

The present analysis assumes that, up to incipient dryout of the evaporator wick, the Creare-type condenser structure is saturated with liquid sodium, and the liquid–vapor (L–V) interface is highly reflective (effective emissivity of ~0.05). This assumption is reasonable, particularly at high electric current (or high condensation mass flux). At low electric current, however, the condenser wick may be partially exposed as the liquid sodium recedes into the 250-μm-wide grooves at its surface.[8] In this case, at $T_{\text{cd}} = 623$ K, a liquid tension of as much as -1.38 kPa may develop at the L–V interface in the condenser structure.

Figure 3 shows a line diagram of the calculated local sodium pressure in a five-tube, PX-3A-type converter operating at $T_{\text{hot}} = 1123$ K and a peak power of 3.7 W_e. The liquid in the condenser wick is at saturation (623 K); thus, the local pressure is ~10 Pa. The large pressure losses in the LSRA and the evaporator wick (predicted to be ~6 kPa) cause a tension in the liquid phase (negative local pressure) at the surface of the evaporator wick.[13] At an evaporator temperature of 1047 K, the sodium saturation pressure is ~34.5 kPa (Fig. 3), whereas the pressure drop due to evaporation of liquid sodium at the evaporator wick surface is only ~60 Pa, when the converter current is 2.4 A (the corresponding sodium mass flow rate is 10.3 g/h).

The sodium vapor flows from the evaporator wick surface to the anode side of the BASE tubes, with negligible pressure losses (<50 Pa). The neutral sodium atoms, emerging from the cathode side of the BASE at 70 Pa, traverse the low-pressure cavity to the condenser. Because the condenser pressure is typically three to four

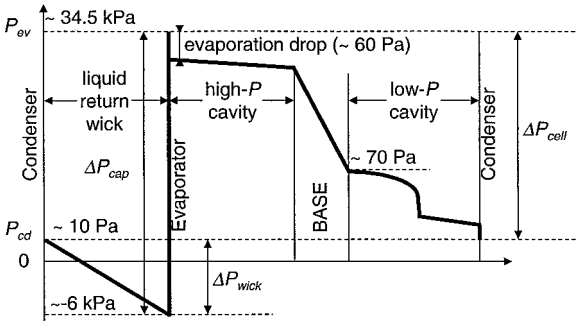

Fig. 3 Line diagram of the local pressures at peak power in a five-tube, PX-3A type, SS converter: $Q_{\text{in}} = 30$ W, $T_{\text{hot}} = 1123$ K, $T_{\text{cd}} = 623$ K, $T_{\text{ev}} = 1047$, and $I = 2.4$ A.

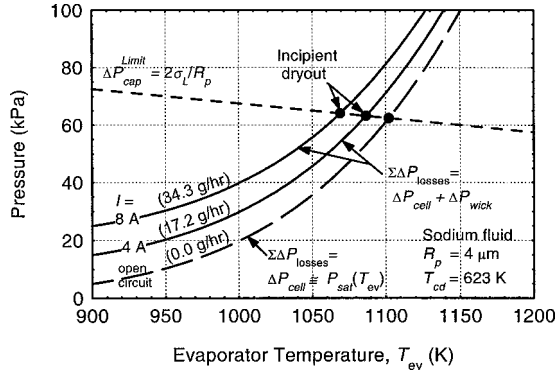

Fig. 4 Capillary limit in the evaporator wick of a five-tube, PX-3A-type, SS converter.

orders of magnitude smaller than the vapor pressure at the evaporator surface, $\Delta P_{\text{cell}} = P_{\text{sat}}(T_{\text{ev}}) - P_{\text{sat}}(T_{\text{cd}}) \approx P_{\text{sat}}(T_{\text{ev}})$, assuming that the Creare condenser structure is saturated with liquid sodium and does not develop a liquid tension.

As indicated earlier, the capillary limit at the surface of the evaporator wick is reached when the radius of curvature of the liquid meniscus in the surface pores, R_c, equals the pore radius R_p:

$$\Delta P_{\text{cap}}^{\text{limit}} = 2\sigma_L / R_p \tag{15}$$

The conditions for incipient dryout in the evaporator wick of a five-tube PX-3A-type converter are shown in Fig. 4. The capillary pressure head at incipient dryout decreases linearly with increasing T_{ev}, due to the decrease in the surface tension of liquid sodium. The sum of the pressure losses in the converter ($\Sigma\Delta P_{\text{losses}} = \Delta P_{\text{wick}} + \Delta P_{\text{cell}}$) increases exponentially with T_{ev} and to a much lesser extent with the converter current (or sodium circulation rate). The intersect of the $\Sigma\Delta P_{\text{losses}}$ curve with the capillary pressure limit curve indicates the condition for incipient dryout (Fig. 4). Open-circuit incipient dryout is predicted at a capillary pressure head of 62 kPa (or $\Delta P_{\text{cell}} = 62$ kPa) and $T_{\text{ev}} = 1102$ K. Increasing the load current (or sodium flow rate) causes incipient dryout of the evaporator wick to occur at a lower evaporator surface temperature (Fig. 4).

Liquid Flow in the LSRA and Evaporator Wick

The flow of liquid sodium in the saturated, isotropic porous structure of the evaporator and of the LSRA is modeled using the Forchheimer-extended Darcy's continuity and momentum balance equations (see Ref. 14):

$$\varepsilon \frac{\partial \rho_L}{\partial t} + \text{div}[\rho_L \boldsymbol{q}] = 0 \tag{16a}$$

$$\frac{1}{\varepsilon}\frac{\partial(\rho_L \boldsymbol{q})}{\partial t} = \rho_L \boldsymbol{g} - \nabla P_L - \frac{\mu_L \boldsymbol{q}}{K} - \frac{C}{\sqrt{K}}\rho_L |\boldsymbol{q}|\boldsymbol{q} \tag{16b}$$

where $\boldsymbol{q}$ is the mean filter (area-averaged) velocity. Because the liquid sodium flow rate in an AMTEC converter is low (typically <25 g/h), Forchheimer's extension could be neglected or treated explicitly in the momentum equations [the fourth term on the right-hand side of Eq. (16b)]. The sintered wick permeability K and the inertia coefficient C are calculated using the Blake–Kozeny equations (see Ref. 15) as

$$K = \frac{d^2}{150}\frac{\varepsilon^3}{(1-\varepsilon)^2}, \qquad C = \frac{1.75}{\sqrt{150}}\frac{1}{\varepsilon\sqrt{\varepsilon}} \tag{17}$$

The characteristic length d is given as[12]

$$d = 2R_p / 0.41 \tag{18}$$

The momentum balance Eqs. (16b) are discretized as

$$\left[\frac{1}{\varepsilon\Delta t}+\frac{\mu_L^{i,j}}{K\rho_L}+\frac{C\left|q_{i,j}^n\right|}{\sqrt{K}}\right](\rho_L q_r)_{i,j}^{n+1}$$

$$=\frac{(\rho_L q_r)_{i,j}^n}{\varepsilon\Delta t}+\frac{(P_L)_{i,j}^{n+1}-(P_L)_{i+1,j}^{n+1}}{(\Delta R_i+\Delta R_{i+1})/2} \tag{19a}$$

$$\left[\frac{1}{\varepsilon\Delta t}+\frac{\mu_L^{i,j}}{K\rho_L}+\frac{C\left|q_{i,j}^n\right|}{\sqrt{K}}\right](\rho_L q_z)_{i,j}^{n+1}$$

$$=\frac{(\rho_L q_z)_{i,j}^n}{\varepsilon\Delta t}-\rho_L g+\frac{(P_L)_{i,j}^{n+1}-(P_L)_{i,j+1}^{n+1}}{(\Delta Z_j+\Delta Z_{j+1})/2} \tag{19b}$$

and can be written in the following form:

$$(\rho_L A_r q_r)_{i,j}^{n+1}=C_r^{i,j}\left[(P_L)_{i,j}^{n+1}-(P_L)_{i+1,j}^{n+1}\right]+S_r^{i,j}$$

$$(\rho_L A_z q_z)_{i,j}^{n+1}=C_z^{i,j}\left[(P_L)_{i,j}^{n+1}-(P_L)_{i,j+1}^{n+1}\right]+S_z^{i,j} \tag{20}$$

The coefficients C_r, C_z, and S_r, and S_z are set equal to zero along the solid boundaries of the evaporator wick and LSRA because there is no sodium flow through these boundaries.

The continuity Eq. (16a) is discretized as

$$(\varepsilon/\Delta t)\left[\rho_L^*\mathrm{Vol}_{i,j}^{n+1}-\rho_L^n\mathrm{Vol}_{i,j}^n\right]+(\rho_L A_r q_r)_{i,j}^{n+1}-(\rho_L A_r q_r)_{i-1,j}^{n+1}$$

$$+(\rho_L A_z q_z)_{i,j}^{n+1}-(\rho_L A_z q_z)_{i,j-1}^{n+1}=0 \tag{21}$$

For the control volume (i, j), located at the surface of the evaporator wick, $(\rho_L A_r q_r)_{i-1,j}^{n+1}=0$ and $(\rho_L A_z q_z)_{i,j}^{n+1}=A_{\mathrm{ev}}^{i,j}(\dot{m}''_{\mathrm{ev}})_{i,j}^*$. The Poisson equation for the liquid pressure in the wick is obtained by substituting Eqs. (20) into Eq. (21). Once the liquid pressure distribution in the evaporator wick is known, the local radius of curvature of the liquid meniscus in the surface pores of the evaporator wick, R_c, is calculated using the extended Pascal relationship, as explained in the next section. The capillary limit is reached when R_c equals R_p.

Liquid Meniscus in the Surface Pores of the Evaporator Wick

The vapor and liquid phases in the surface pores of the evaporator wick are thermally and hydrodynamically coupled through Eq. (6) and the normal momentum jump condition. The computational control volumes $\mathrm{Vol}_{i,j}$ are kept fixed (independent of time), except those at the surface of the evaporator wick. The interfacial liquid volume is a function of the pore void fraction α_p as

$$\varepsilon\mathrm{Vol}_{i,j}^{n+1}=\varepsilon\mathrm{Vol}_0^{i,j}-\mathrm{Vol}_p^{i,j}\times(\alpha_p)_{i,j}^{n+1} \tag{22}$$

where $\mathrm{Vol}_p^{i,j}=(\frac{2}{3})R_p\varepsilon A_{\mathrm{ev}}^{i,j}$ is the volume of the hemispherical pores at the conical evaporator wick surface and Vol_0 is the volume of the interfacial control volume when the L–V interface in the pores is flat (the wick surface pores are fully saturated with liquid and $R_c=+\infty$). The pore void fraction is a geometrical function of the cosine of contact angle of the liquid meniscus ($\mu_c=R_p/R_c$) (Ref. 16) as

$$\alpha_p=\left(1/\mu_c^3\right)\left[1-\left(1+\mu_c^2/2\right)\sqrt{1-\mu_c^2}\right] \tag{23}$$

The cosine of the contact angle of the liquid meniscus is related to the liquid and vapor pressures on both sides of the L–V interface by the momentum jump condition[17]:

$$(P_L)_{i,j}^{n+1}-P_a^*+(2\sigma_L/R_p)(\mu_c)_{i,j}^{n+1}$$

$$+(1/\varepsilon\rho_L-1/\rho_V)\left[(\dot{m}''_{\mathrm{ev}})_{i,j}^*\right]^2=0 \tag{24}$$

The maximum capillary pressure head developed at the surface of the evaporator wick occurs when the local radius of curvature of the liquid meniscus equals the geometrical radius R_p. At such conditions, the void fraction in the wick interfacial pores equals unity, which is used herein to indicate incipient dryout or capillary limit in the evaporator wick.

When Eqs. (22–24) are combined, the change in the liquid volume in the evaporator wick interfacial control volume (i, j) becomes a linear function of the local liquid pressure:

$$\varepsilon\mathrm{Vol}'_{i,j}=\frac{\mathrm{Vol}_p^{i,j}}{2\sigma_L/R_p}\left(\frac{\partial\alpha_p}{\partial\mu_c}\right)_{i,j}^*\left\{\left(P_L^*\right)_{i,j}+\left(P'_L\right)_{i,j}\right.$$

$$\left.+\frac{2\sigma_L}{R_p}(\mu_c)_{i,j}^*-P_a^*+\left(\frac{1}{\varepsilon\rho_L}-\frac{1}{\rho_V}\right)^*\left[(\dot{m}''_{\mathrm{ev}})_{i,j}^*\right]^2\right\} \tag{25}$$

The vapor pressure in the evaporator wick cavity, P_a, is explicitly discretized in Eqs. (24) and (25); it is an explicit function of the evaporator wick surface temperature and the electrical current (or sodium flow rate) in the converter [see Eq. (9)].

Sodium Flow Rate in Converter

The sodium flow rate in the converter is directly proportional to the electrical current I as

$$\dot{m}=N_B(MI/F)=N_B(MV_L/FR_L) \tag{26}$$

The external load voltage, which equals the sum of the electrical potentials developed in the BASE tubes minus the electric losses, is calculated by the electrical circuit model in APEAM.[5] The electrical potential developed in the BASE tubes is a function of P_a and of the sodium vapor pressure at the interface between the cathode electrode and the BASE. The latter is calculated by the vapor pressure loss model in APEAM.[3] The pressure drop across the cathode electrode is typically expressed in terms of an empirical dimensionless factor G_E, which is determined experimentally (see Table 1).

Results and Discussion

The coupled conical evaporator/APEAM model is used to predict the performance of the PX-3A converter (Fig. 1). The design parameters of this converter are given in Table 1. The evaporator wick is 4.9 mm in diameter, is 21.5 mm-high, and is encased in a 0.71-mm-thick SS tube, which is surrounded by three nickel rings (1.1 mm thick) (Fig. 5a). The deep conical evaporator of this converter has an apex half angle, $\theta\sim 8$ deg, and its base is situated 5.2 mm above the BASE support plate (Fig. 5a). The calculated thermal conductance of the 5.2-mm-high standoff wall and surrounding nickel rings is 0.43 W/K at 1100 K. The felt-metal LSRA is 3.2 mm in diameter and ~60 mm long. In the experiment, the converter was tested in the vertical position, with the condenser in the downward position, so that the sodium flow to the evaporator wick was against gravity.[1] The PX-3A converter was subjected to a fixed cold-side temperature ($T_{\mathrm{cd}}=623$ K) and $T_{\mathrm{hot}}=1023$, 1123, and 1173 K. The permeabilities of the LSRA (64% porous) and of the evaporator wick (42% porous) are taken as 2.0×10^{-12} m^2 and 2.6×10^{-13}m^2, respectively,[18] and the effective pore radius in the evaporator wick is taken as 4 μm.

The predicted electric power is in good agreement with measurements (Fig. 6a). Incipient dryout at the evaporator wick surface is predicted to occur at $T_{\mathrm{hot}}=1138$ K. Thus, it is possible that the converter was capillary limited when operated at $T_{\mathrm{hot}}=1173$ K. The predicted evaporator temperature is ~50 K higher than measurements (Fig. 6b); however, the slope of the predicted T_{ev}–I curve is identical to that of the measurements. The estimated uncertainty in the temperature measurements is ±15 K (Ref. 1). As indicated by the dashed lines in Fig. 6a, changing the surface of the evaporator from a deep cone ($\theta=8$ deg) to flat ($\theta=90$ deg) decreases the peak electrical power of the converter by only 1.5%.

Effect of Sodium Vapor Leakage on Performance of PX-3A Cell

A process that may explain the difference between the predicted and measured evaporator temperatures in PX-3A is sodium vapor

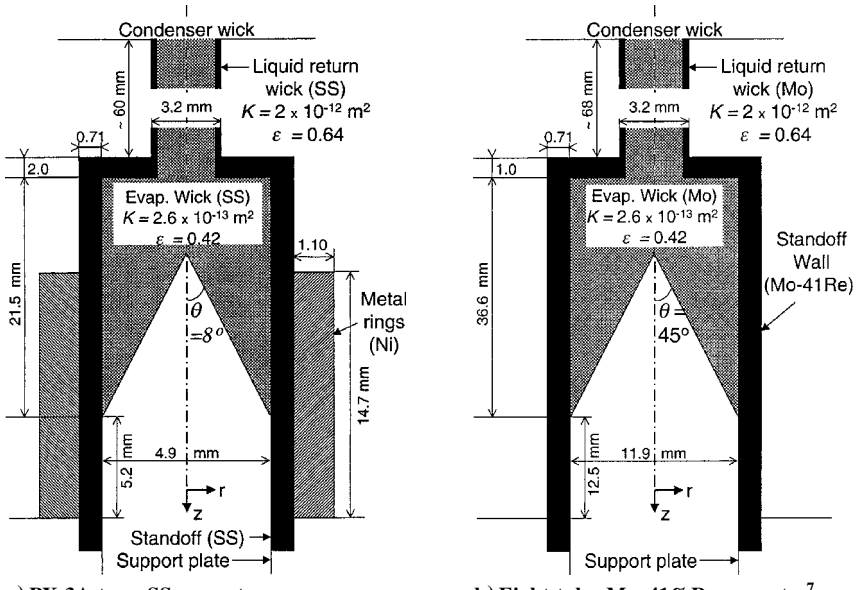

a) PX-3A-type, SS converter b) Eight-tube, Mo–41% Re converter[7]

Fig. 5 LSRA and evaporator structure design (not to scale).

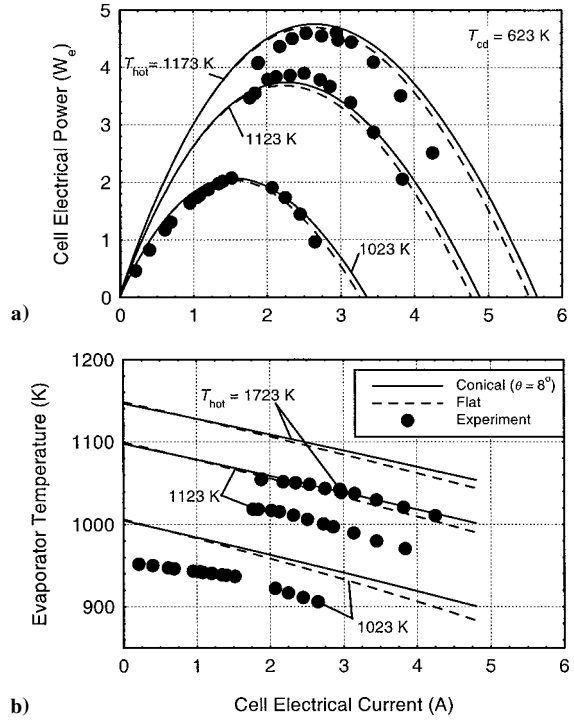

Fig. 6 Comparison of predictions and measurements for the PX-3A converter.

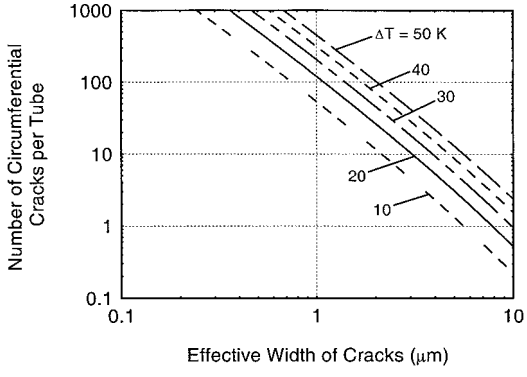

Fig. 7 Number of circumferential cracks per tube to bring the PX-3A evaporator temperature down by a specified ΔT: T_{hot} = 1123 K, T_{cd} = 623 K, I = 2.5 A, and θ = 8 deg.

leakage through the BASE membrane or braze with the metal support plate (Fig. 1a).[19] Such vapor leakage would increase the circulating sodium mass flow rate, beyond that diffusing through the BASE membranes (which is directly proportional to the electric current). As shown in Fig. 6b, the larger the electric current (or the evaporator mass flow rate), the lower is the evaporator surface temperature. At a fixed T_{hot}, and in the absence of leakage, the evaporator temperature decreases almost linearly with the generated vapor mass flow rate (or the electric current). This is because the thermal energy consumed in the vaporization of the liquid Na is proportional to the sodium flow rate and must be conducted up the standoff structure and the metal rings to the evaporator wick (Fig. 1a).

The evaporation rate of sodium would be higher than the diffusion rate through the BASE in two possible situations: 1) when the temperature margin in the converter is negative, causing condensation of sodium inside the BASE tubes and 2) when there is a vapor leakage between the hot plenum to the low-pressure cavity (Fig. 1a). A preliminary analysis of the latter was performed, assuming a vapor leakage path through a number of circumferential cracks, either in the ceramic BASE tubes and/or the ceramic–metal brazes. Braze joints could fail as a result of developing circumferential cracks, which has been observed recently in postexaminations of PX converters performed at the Jet Propulsion Laboratory.[19] The pressure drop through circumferential cracks is calculated[3] as a function of the number of cracks to bring the evaporator temperature down by a fixed ΔT, when $T_{hot} = 1123$ K and the electric current is the same as that measured at the peak electric power in PX-3A (2.5 A, Fig. 6a). As shown in Fig. 7, one 7-μm-wide crack, or ten 3-μm-wide cracks per BASE tube would allow a vapor leakage flow rate of 4.4 g/h, lowering the calculated evaporator temperature by 20 K. This vapor leakage rate is equivalent to a 1.03 A increase in the electric current to 3.53 A; thus, the evaporator would be circulating sodium at a flow rate of 15.1 g/h.

The circulation of the excess sodium due to a leakage negatively impacts the conversion efficiency. The latter was estimated at the measured electrical power output of the PX-3A converter in Fig. 6a, by correcting the heat input predicted by APEAM for the additional heat required to vaporize the excess sodium. Results are presented in Fig. 8 for $T_{hot} = 1123$ K and 4-μm-wide circumferential cracks. As Fig. 8 indicates, the effect of the leakage of sodium vapor on the

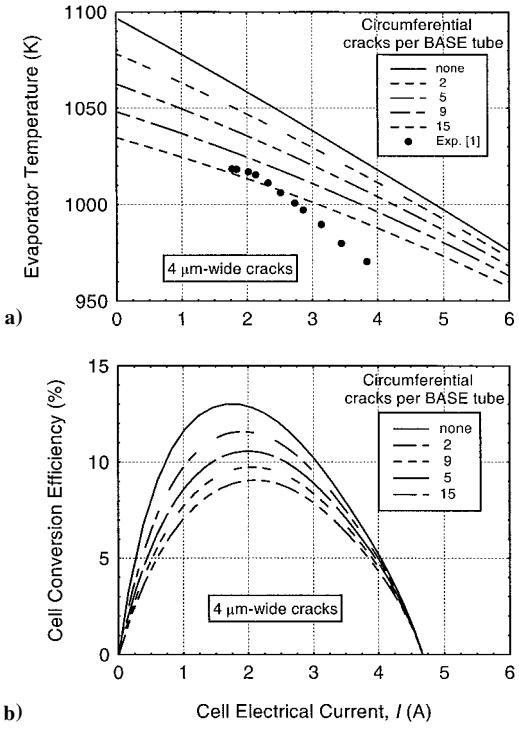

Fig. 8 Effect of sodium vapor leakage on the conversion efficiency of PX-3A converter: T_{hot} = 1123 K, T_{cd} = 623 K, and θ = 8 deg.

evaporator temperature is more pronounced at low converter current (Fig. 8a). When assuming no sodium vapor leakage, the PX-3A converter had a predicted peak efficiency of 13% at $T_{hot} = 1123$ K and $I = 1.75$ A (Fig. 8b). However, as shown in Fig. 8b, the existence of two, 4-μm-wide cracks per BASE tube or in their brazes with the metal support plate drops the converter's peak efficiency by 1.5 points (to 11.5%, with a corresponding sodium leakage rate of 2.5 g/h). As Fig. 8b also shows, more dramatic drops in the converter efficiency could result at higher leakage rates.

Heat Transfer in PX-3A Converter

Figure 9 shows the predicted heat flow and structure temperatures in the PX-3A converter, when operating at its peak electrical power and $T_{hot} = 1173$ K. Experimental measurements are shown in parentheses. Of the total thermal power input, $Q_{in} = 33.65$ W, the conduction stud transported 15.86 W (47%) and the plenum wall conducted 15.85 W (47%) to the BASE tubes' support plate. Only 1.94 W (6%) are radiated from the hot plate into the high-pressure cavity. Most of the radiant heat transfer is absorbed by the five BASE tubes (1.77 W), and only 0.19 W is absorbed at the inner surface of the evaporator standoff wall. About 76% of the heat transported through the conduction stud is used to evaporate liquid sodium at the evaporator wick surface (12.1 W). The temperature of the BASE support plate is only 26 K lower than the hot plate.

A total of 21.86 W is removed at the condenser (Fig. 9), which comprises 1) the latent heat of condensation of sodium vapor in the low-pressure cavity (13.4 W), 2) heat conduction up the side wall (4.38 W), 3) parasitic radiation losses from the BASE tubes and other structures to the condenser surface (0.91 W), and 4) heat conduction up the LSRA to the condenser (3.17 W).

The calculated heat losses by radiation from the cell wall to the surrounding Min-K insulation in the experiment are 6.58 W. The sum of heat transfer rates 2–4 and of the heat losses from the wall by radiation (6.58 W) represents the total parasitic heat losses in the PX-3A converter (15.04 W), which amount to as much as 44.7% of the total input thermal power (33.65 W). Reducing the parasitic heat losses by 50% would increase the conversion efficiency from ~14 to ~19%. The next section investigates the effect of changing the cone angle of the evaporator wick on its performance.

Table 2 Evaporator surface area in a PX-3A-type converter

	θ, deg				
Area	8	16	30	45	90 (flat)
A_{ev}, mm^2	135.5[a]	68.4	37.71	26.67	18.86
Area ratio	7.2[a]	3.6	2.0	1.414	1

[a]PX-3A converter tested in vacuum.[1]

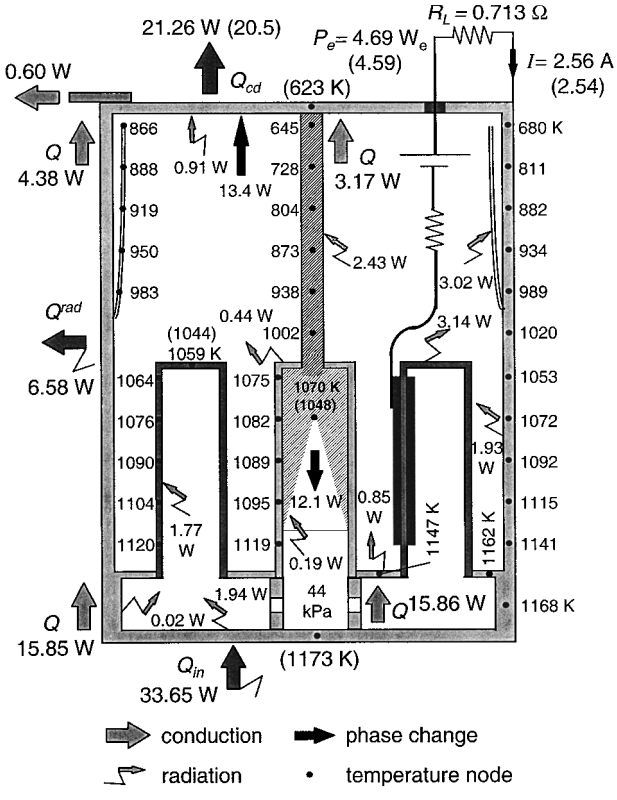

Fig. 9 Predicted heat flow and structure temperatures in the PX-3A converter operating at peak electrical power 4.7 We; tested converter had 8-deg conical evaporator wick (experimental measurements shown in parentheses).

Performance of Conical Evaporators

The effect of changing the cone angle of the PX-3A evaporator wick ($8 \le \theta \le 90$ deg) on its performance is investigated. The length of the evaporator standoff (5.2 mm) is maintained constant in all cases analyzed. Figure 10 shows the predicted wick surface temperature, vaporization mass flux, and vapor pressure along the evaporator surface, for a constant mass flow rate of 10.73 g/h (an electrical current $I = 2.5$ A). In all cases, the wick surface temperature is essentially uniform, within ± 1 K (Fig. 10a). The liquid sodium vaporization, however, occurred mostly in the outermost region of the evaporator wick surface, near the standoff wall (Fig. 10b). The effective vapor pressure at the surface of the flat evaporator, 33.5 kPa, is the lowest (Fig. 10c). By contrast, the shallow cone evaporators ($\theta = 45$ and 30 deg) exhibited the most uniform wick surface temperature and vaporization mass flux. The 30-deg shallow conical evaporator wick, which has twice the surface area of the flat evaporator (Table 2), provided a 1.2 kPa higher vapor pressure than the latter.

The deep conical evaporators ($\theta = 8$ and 16 deg), with the highest surface area (7.2 and 3.6 times that of the flat evaporator, respectively), exhibited the best performance (Figs. 10a and 10b). However, the long conduction path to the apex of the evaporator wick resulted in a cooler surface temperature near the apex, causing condensation of sodium vapor (Fig. 10b), as commonly observed in heat pipes. As a result, the performance of a deep conical evaporator does not increase proportionally with its surface area.

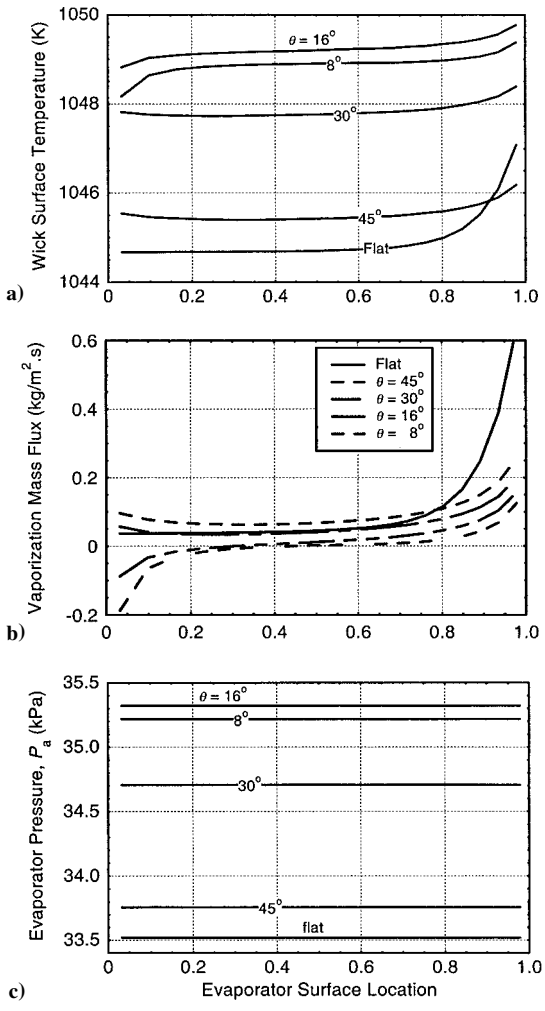

Fig. 10 Effect of the apex half angle on the performance of the evaporator wick in PX-3A converter: T_{hot} = 1123 K, T_{cd} = 623 K, I = 2.5 A, or $\dot{m}_l$ = 10.73 g/h.

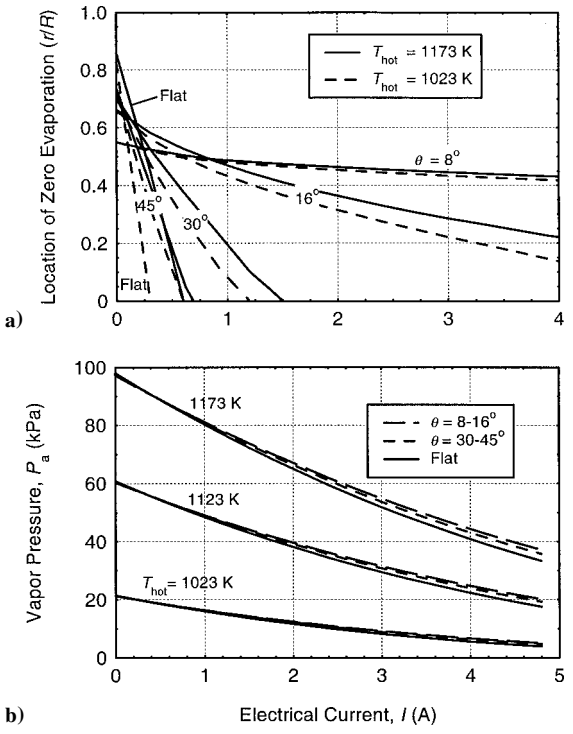

Fig. 11 Effects of the apex half angle, electrical current, and hot side temperature in PX-3A converter on the vapor pressure and the location of zero evaporation in the surface of the evaporator wick: T_{cd} = 623 K.

Figure 11 shows that, at typical electric currents ($I > 1.5$ A), the flat and shallow conical evaporators do not experience any condensation on their surface (or heat pipe effect). The 16-deg conical evaporator, however, experienced condensation over 10% of its surface, whereas the 8-deg conical evaporator experienced condensation over 20% of its surface (Fig. 11a). Note that this heat pipe effect is not strongly affected by the operating temperature of the converter. The condensate near the apex of the deep conical evaporators may form a liquid bridge, hence, reducing further the available surface for evaporation. This phenomenon, however, is outside the scope of this study.

The decrease in the total evaporation rate due to condensation of sodium vapor in the deep conical evaporators is largely offset by the large surface area available for evaporation, compared to a flat evaporator (a factor 7.2 for $\theta = 8$ deg). For the same sodium mass flow rate or electrical current, the deep conical evaporators provide a sodium vapor pressure that is 1.7–1.8 kPa higher than in a flat evaporator (Fig. 10c). The performance of the 8- and 16-deg conical evaporators is very similar, with the latter slightly better at converter currents below ~3 A (Fig. 10c). The next section investigates incipient dryout (or capillary limit) in deep ($\theta = 8$ deg) and shallow ($\theta = 45$ deg) conical evaporator wicks.

Incipient Dryout in the Evaporator Wick of a PX-3A-Type Converter

The shape of the evaporator wick also affects its ability to circulate the liquid sodium back from the condenser. The sodium working fluid is circulated in the converter by the capillary pressure head developed at the surface of the evaporator wick [Eq. (24)]. The present analysis assumes that, up to incipient dryout, the Creare condenser is saturated with liquid ($R_c = +\infty$).

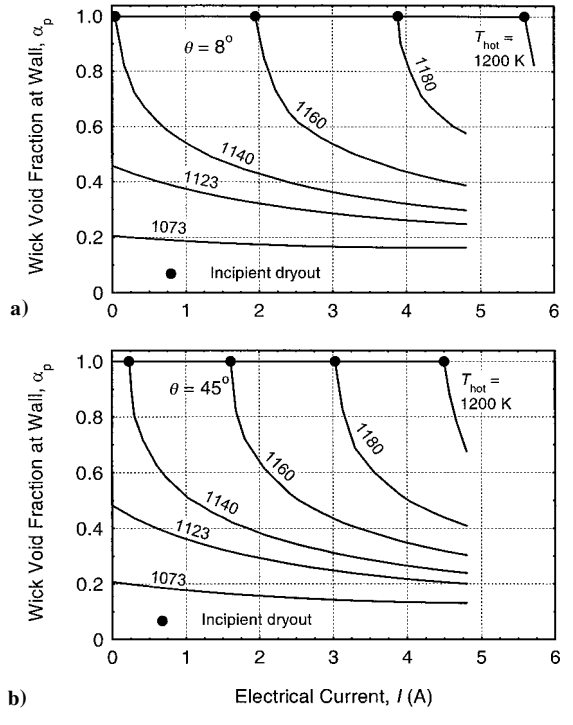

Fig. 12 Effects of the electrical current and hot side temperature on incipient dryout of the evaporator wick in the PX-3A converter: T_{cd} = 623 K.

Figure 12 shows the predicted void fraction in the evaporator wick surface at the standoff wall, as a function of the electrical current and hot-side temperature, for 8- and 45-deg conical evaporators. Dryout ensues when the electrical current (or the sodium flow rate) decreases below a cutoff value, which depends on the hot-side temperature. For example, a 45-deg conical evaporator is

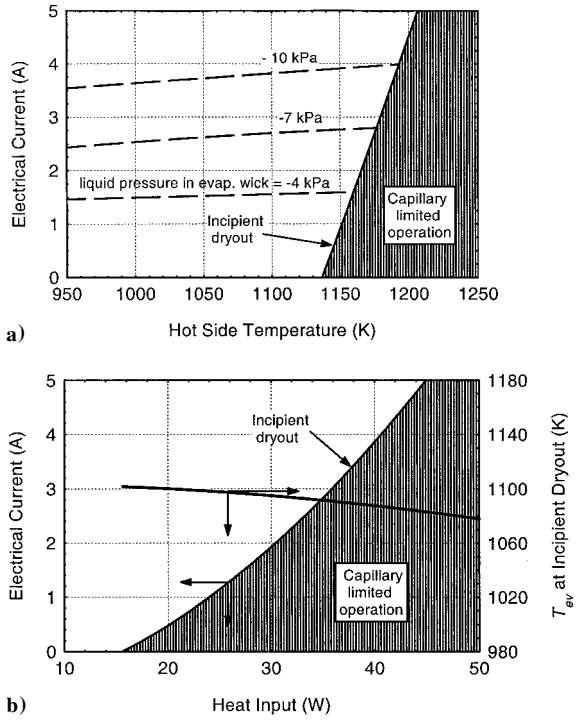

Fig. 13 Predicted conditions of incipient dryout and liquid tension in the evaporator wick of PX-3A converter: θ = 45 deg, T_{cd} = 623 K, and R_p = 4 μm.

capillary limited when $I < 1.6$ A and the hot-side temperature is 1160 K. Decreasing the electrical current increases the evaporator surface temperature (Fig. 11b), resulting in a higher vapor pressure and lower surface tension of liquid sodium. This increase in the sodium vapor pressure, an exponential function of temperature, largely offsets the decrease in the liquid pressure losses in the converter (which are proportional to the electrical current), causing a local dryout. Figures 12a and 12b show that a 8-deg, conical evaporator would experience incipient dryout at a 0.2–1.0 A higher electric current than a shallow, 45-deg conical evaporator. Note that the liquid sodium in the evaporator wick, below the L–V interface, is always in tension (Fig. 13a).

The operation domain in which the PX-3A converter with a 45-deg conical evaporator is capillary limited is indicated by the shaded area in Fig. 13. Results suggest that the converter may operate at a hot-side temperature up to 1136 K (an input thermal power up to 16 W) and any electrical current, without encountering the capillary limit. The evaporator wick is capillary limited at $T_{hot} = 1173$ K ($Q_{in} = 36$ W) and $I < 3.0$ A. At $I = 3.0$ A, the maximum liquid tension just below the evaporator wick surface is -7.5 kPa (Fig. 13a).

The isotension contours in Fig. 13a indicate a liquid tension as high as -4 kPa near the evaporator wick surface when the electrical current is as low as 1.7 A. The liquid tension in the evaporator wick could be as high as -10 kPa when the electrical current $I \sim 3.7$ A. Many experiments have validated the existence of high tension in the liquid phase in porous structures.[20,21] Anderson et al.[13] have predicted tensions as high as -5 kPa in liquid sodium in a wick-pumped AMTEC.

Figure 13b also shows that at incipient dryout the surface temperature of the evaporator wick reaches 1102 K, when the input thermal power $Q_{in} = 16$ W. Below or at this input thermal power, however, the converter may operate at any electrical current without encountering the capillary limit. This is because increasing the current (or the sodium mass flow rate) decreases the evaporator surface temperature and, hence, increases the radius of curvature of the liquid meniscus in the surface pores. At a fixed T_{hot}, the evaporator temperature decreases almost linearly with the vapor mass flow rate because of the increased energy consumption in the vaporization of liquid sodium (Fig. 6b).

At a fixed sodium mass flow rate, increasing the hot side temperature (or the input thermal power) increases the evaporator temperature, resulting in a higher vapor pressure and lower surface tension. At $T_{hot} = 1167$ K ($Q_{in} = 30$ W) and a current $I = 2$ A, $T_{ev} = 1096$ K, and the evaporator wick is capillary limited. At this temperature, the maximum capillary pressure head equals the sum of the sodium evaporator pressure (57.7 kPa) and the liquid pressure losses, $\Delta P_{wick} = 4.9$ kPa (Figs. 13a and 13b). On the other hand, increasing the electrical current decreases the evaporator temperature and the sodium pressure and increases the liquid surface tension. The increase in electric current also increases the liquid pressure losses in the wick, which is largely offset by the exponential decrease in vapor pressure. The lower vapor pressure is indicative of a decrease in the void fraction in the surface pores of the evaporator wick, thus avoiding the capillary limit. The higher the hot-side temperature or input thermal power, the higher is the electrical current at incipient dryout, and the lower is the evaporator temperature, to balance the increase in the liquid pressure losses in the LSRA and in the evaporator wick.

Incipient Dryout in the Evaporator Wick of the Mo-41%Re Converter

The design and operation parameters of the Mo–41%Re converter[7] are given in Table 1. This converter has eight BASE tubes having 38.1 mm-long W/$Rh_{1.5}$ electrodes. The evaporator wick of this converter, shown in Fig. 5b, has an apex half angle, $\theta = 45$ deg, and an effective pore radius of 4 μm. The estimated thermal conductance of the 12.5-mm-long Mo–41%Re standoff wall is 0.15 W/K at 1100 K, which is only 35% of that in the PX-3A-type converter. This bare standoff wall helped maintain a temperature margin $\Delta T > 20$ K. The LSRA and evaporator wicks of the refractory converter are made of molybdenum felt that is sintered at 1373 K or above. The wick parameters are given in Fig. 5b.

The operation domain in which the Mo–41%Re converter is capillary limited is indicated by the shaded area in Fig. 14. This converter may operate at a hot-side temperature up to 1150 K (a input thermal power up to 22 W) and any electric current without encountering the capillary limit. At $T_{hot} = 1173$ K ($Q_{in} = 27$ W), the evaporator wick

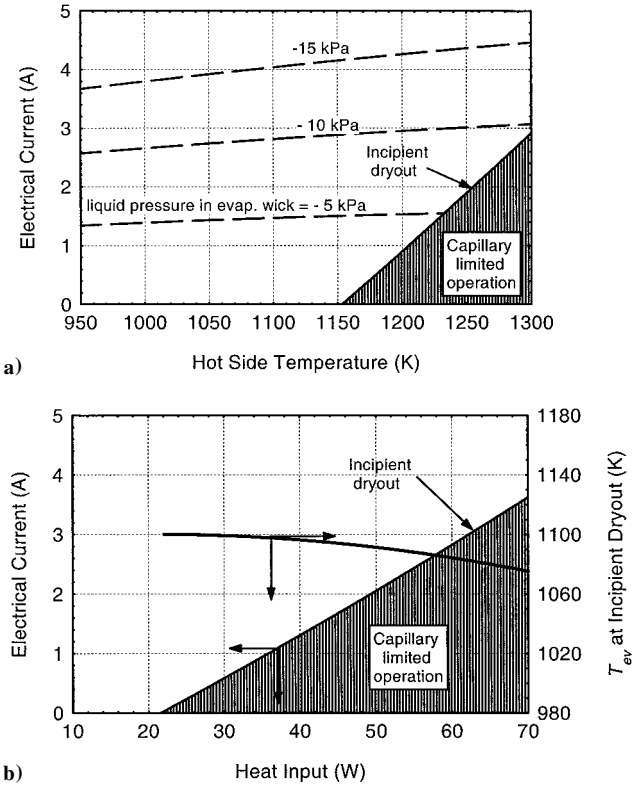

Fig. 14 Predicted conditions for incipient dryout and liquid tension in the evaporator wick of the eight-tube, Mo–41% Re converter: θ = 45 deg, T_{cd} = 640 K, and R_p = 4 μm.

becomes capillary limited when $I < 0.8$ A. At this cutoff current, the maximum liquid tension just below the evaporator wick surface is -1.4 kPa (Fig. 14a).

When the electrical current is small, the liquid pressure losses in the LSRA and evaporator wick are negligible. In addition, the heat removed by vaporization at the evaporator surface is small, compared to the heat transfer to the evaporator structure by conduction and radiation. As a result, at low current, incipient dryout in the evaporator wick of both the SS PX-3A converter and the Mo–41%Re converter occurs at almost the same $T_{hot} \sim 1150$ K ($T_{ev} = 1102$ K) (Figs. 13 and 14).

At large electrical current, the evaporator surface temperature is controlled mostly by the conductance of the evaporator standoff wall and by the heat removal by vaporization. The latter is proportional to the total sodium mass flow rate, or the electrical current times the number of BASE tubes in the converter [see Eq. (26)]. Because of the low thermal conductance of its evaporator standoff wall (0.15 W/K vs 0.43 W/K in the five-tube PX-3A converter), the refractory converter has a more extended domain of operation in which it is not capillary limited. At a current $I = 2$ A, the refractory converter may operate at a hot-side temperature up to 1254 K, whereas the PX-3A-type converter can only operate up to $T_{hot} = 1167$ K, before encountering the capillary limit (Figs. 13a and 14a). The slope of the incipient dryout line bordering the shaded area in which the converter is capillary limited can, therefore, be controlled by changing the conductance of the evaporator standoff structure. The intersection of this line with the zero current axis is essentially dependent on the effective pore size of the evaporator wick (Fig. 4).

Other Operation Limits in Vapor Anode, Multitube Converters

Results presented in Figs. 13 and 14 show that incipient dryout in the PX-3A and the Mo–41%Re converters occurs when the hot-side temperature exceeds 1136 and 1150 K, respectively. At such temperatures, however, the converter operation is always limited by one or more of the following design requirements: 1) the temperature of the BASE tubes' braze joints ≤ 1123 K, 2) the temperature of the evaporator wick ≤ 1023 K, and 3) the temperature margin in the converter, $\Delta T \geq 20$ K (Refs. 6, 9, and 18).

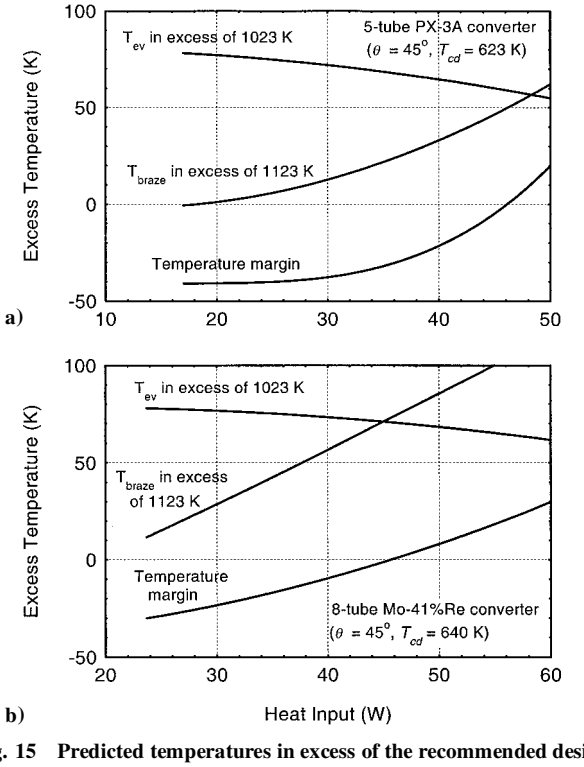

Fig. 15 Predicted temperatures in excess of the recommended design values for the evaporator surface, the BASE brazes, and the temperature margin at incipient dryout.

Figure 15 shows that at incipient dryout, both in the PX-3A and the refractory converters, the evaporator temperature limit is always exceeded by more than 50 K. In addition, the temperature margin is negative up to a heat input of 46 W in both converters. A temperature margin, $\Delta T > 20$ K, is achieved when $Q_{in} > 50$ W in the PX-3A converter and when $Q_{in} > 56$ W in the refractory converter (Fig. 15). Furthermore, the BASE brazes temperature is always above its recommended design value of 1123 K, except at very low input thermal power ($Q_{in} < 20$ W). Therefore, in both the PX-3A and the refractory converters, two or more of the design temperature limits are exceeded before incipient dryout in the evaporator wick.

Conclusions

A detailed, two-dimensional thermal–hydraulic model of conical and flat evaporators and of the LSRA in vapor anode AMTEC converters is developed and coupled to the integrated converter model APEAM. The evaporator wick model predicts the capillary limit (or incipient dryout) as well as the liquid tension at the evaporator wick surface, as functions of the hot-side temperature (or input thermal power) and load electrical current.

Results showed that the surface temperature of the evaporator wick is essentially uniform, varying only within 2 K for both flat and conical evaporators. For a given sodium mass flow rate, the flat evaporator provides the lowest vapor pressure and lowest liquid pressure losses. The deep cone evaporators ($\theta = 16$ and 8 deg), with a much larger surface area (3.6 and 7.2 times that of the flat evaporator, respectively), exhibit good performance, despite the partial condensation of sodium vapor over 10–20% of their surfaces, near the apex. The effect of sodium condensation is largely offset by the large surface area available for evaporation. The deep 8-deg conical evaporator wick, however, reaches the capillary limit (or incipient dryout) at 2–10 K lower hot-side temperature or 0.25–1.0 A lower electrical current than a shallow 45-deg conical evaporator wick.

The conditions for incipient dryout in the conical evaporators (45-deg apex half angle) of a five-BASE-tube, PX-3A SS converter and of a recently developed eight-BASE-tube Mo–41%Re converter were also investigated. Results showed that incipient dryout and the highest liquid sodium tension in the evaporator wick surface occurred at the standoff wall. Incipient dryout of the evaporator wick surface occurs when either the electrical current (or sodium flow rate) is below a cutoff value and/or the hot-side temperature is above a certain value.

Results indicated that incipient dryout in the evaporators of the PX-3A and the Mo–41%Re converters can be avoided at all possible operating electrical current when the input thermal power is kept below 16 W (or $T_{hot} < 1136$ K) and 22 W (or $T_{hot} < 1150$ K), respectively. Open-circuit incipient dryout in either converter occurs when the evaporator wick surface temperatures at the input thermal powers indicated earlier are ≥ 1102 K. This cutoff surface temperature value was for an effective pore size of the evaporator wick, $R_p = 4$ μm, and would change with R_p.

At the same electrical current, increasing Q_{in} causes incipient dryout in the refractory converter to occur at a higher hot-side temperature than in the PX-3A converter. Note, however, that incipient dryout in the evaporator wick is not the limiting event in either converter because all other operational temperature limits would be exceeded a priori. At incipient dryout, the calculated evaporator temperature exceeds the recommended value of 1023 K (to slow grain growth in the evaporator wick) by more than 50 K in both converters. Furthermore, the temperature margin in both converters is either negative or below the recommended value of +20 K. Finally, the BASE brazes temperature in both converters exceeds its recommended value of 1123 K for all input thermal power values in excess of 20 W.

Acknowledgment

This research is funded by the University of New Mexico's Institute for Space and Nuclear Power Studies.

References

[1]Merrill, J., Schuller, M. J., and Huang, L., "Vacuum Testing of High-Efficiency Multitube AMTEC Converters: February 1997–October 1997," *Proceedings of Space Technology and Applications International Forum (STAIF-98)*, edited by M. S. El-Genk, AIP CP-420, Vol. 3, American Inst. of Physics, New York, 1998, pp. 1613–1620.

[2]Cole, T., "Thermoelectric Energy Conversion with Solid Electrolytes," *Science*, Vol. 221, No. 4614, 1983, pp. 915–920.

[3]Tournier, J.-M., and El-Genk, M. S., "Sodium Vapor Pressure Losses in a Multitube, Alkali Metal Thermal-to-Electric Converter," *Journal of Thermophysics and Heat Transfer*, Vol. 13, No. 1, 1999, pp. 117–125.

[4]Tournier, J.-M., and El-Genk, M. S., "Radiation Heat Transfer in Multitube, Alkali Metal Thermal-to-Electric Converter," *Journal of Heat Transfer*, Vol. 121, No. 1, 1999, pp. 239–245.

[5]Tournier, J.-M., and El-Genk, M. S., "An Electric Model of a Vapor-Anode, Multi-Tube Alkali-Metal Thermal-to-Electric Converter," *Journal of Applied Electrochemistry*, Vol. 29, No. 11, 1999, pp. 1263–1275.

[6]El-Genk, M. S., and King, J. C., "Performance Analyses of a Nb-1Zr/C-103, Vapor Anode, Multi-Tube Alkali Metal Thermal-to-Electric Conversion Cell," *Journal of Energy Conversion and Management*, Vol. 42, No. 6, 2001, pp. 721–739.

[7]El-Genk, M. S., and Tournier, J.-M., "Analysis of a Vapor Anode, Multi-Tube, Potassium Refractory AMTEC Converter for Space Applications," *Proceedings of Space Technology and Applications International Forum (STAIF-2001)*, edited by M. S. El-Genk, AIP CP-552, Vol. 1, American Inst. of Physics, New York, 2001, pp. 1066–1075.

[8]Crowley, C. J., and Izenson, M. G., "Condensation of Sodium on a Micromachined Surface for AMTEC," *Proceedings of the 10th Symposium on Space Nuclear Power and Propulsion*, edited by M. S. El-Genk and M. D. Hoover, AIP CP-271, Vol. 2, American Inst. of Physics, New York, 1993, pp. 897–904.

[9]Sievers, R. K., Rasmussen, J. R., Borkowski, C. A., Hendricks, T. J., and Pantolin, J. E., "PX-5 AMTEC Converter Development," *Proceedings of Space Technology and Applications International Forum (STAIF-98)*, edited by M. S. El-Genk, AIP CP-420, Vol. 3, American Inst. of Physics, New York, 1998, pp. 1479–1485.

[10]Patankar, S. V., *Numerical Heat Transfer and Fluid Flow*, Hemisphere, Washington, DC, 1980, pp. 79–109.

[11]Cheng, P., "Heat Transfer in Geothermal Systems," *Advanced Heat Transfer*, Vol. 14, 1978, pp. 1–105.

[12]Chi, S. W., *Heat Pipe Theory and Practice*, Hemisphere, Washington, DC, 1976, Chap. 2, pp. 47–51.

[13]Anderson, W. G., Bland, J. J., Ivanenok, J. F., III, and Sievers, R. K., "Design of a Wick-Pumped, Vapor-Fed AMTEC System," *Proceedings of the 28th Intersociety Energy Conversion Engineering Conference*, Vol. 1, American Chemical Society, Washington, DC, 1993, pp. 835–841.

[14]Scheidegger, A. E., *The Physics of Flow through Porous Media*, 3rd ed., Univ. of Toronto Press, Toronto, 1974, pp. 152–170.

[15]Ergun, S., "Fluid Flow Through Packed Columns," *Chemical Engineering Progress*, Vol. 48, No. 2, 1952, pp. 89–94.

[16]Seo, J. T., and El-Genk, M. S., "A Transient Model for Liquid-Metal Heat Pipes," *Space Nuclear Power Systems 1988*, edited by M. S. El-Genk and M. D. Hoover, Vol. 9, Orbit, Malabar, FL, 1989, pp. 405–418.

[17]Delhaye, J.-M., "Jump Conditions and Entropy Sources in Two-Phase Systems—Local Instant Formulation," *International Journal of Multiphase Flow*, Vol. 1, 1974, pp. 395–409.

[18]Hunt, T. K., Sievers, R. K., Ivanenok, J. F., Pantolin, J. E., and Butkiewicz, D. A., "Capillary Pumped AMTEC Module Performance," *Proceedings of the 28th Intersociety Energy Conversion Engineering Conference*, Vol. 1, American Chemical Society, Washington, DC, 1993, pp. 849–854.

[19]Shields, V. B., Kisor, A. K., Fiebig, B., Willians, R. M., Ryan, M. A., and Homer, M. L., "Metallurgical Examination of an AMTEC Unit," *Proceedings of Space Technology and Applications International Forum (STAIF-2001)*, edited by M. S. El-Genk, AIP CP-552, Vol. 2, American Inst. of Physics, New York, 2001, pp. 1094–1099.

[20]Hayward, A. T. J., "New Law for Liquids: Don't Snap, Stretch!" *New Scientist*, Vol. 45, No. 686, 1970, pp. 196–199.

[21]Apfel, R. E., "The Tensile Strength of Liquids," *Scientific American*, Vol. 227, No. 6, 1972, pp. 58–71.